Strained InGaAs/GaPAsSb heterostructures grown on GaAs (001) for optoelectronic applications in the 1100–1550 nm range

W. Braun, P. Dowd, C.-Z. Guo, S.-L. Chen, C. M. Ryu, U. Koelle, S. R. Johnson, Y.-H. Zhang, J. W. Tomm, T. Elsässer, and D. J. Smith

Articles you may be interested in

Highly tensile-strained, type-II, Ga 1 − x In x As / GaSb quantum wells
Appl. Phys. Lett. 96, 062109 (2010); 10.1063/1.3303821

Comparison of GaNAsSb and GaNAs as quantum-well barriers for GaInNAsSb optoelectronic devices operating at 1.3 – 1.55 µ m
J. Appl. Phys. 96, 6375 (2004); 10.1063/1.1807028

Molecular beam epitaxial growth and characterization of strain-compensated Al 0.3 In 0.7 P/InP/Al 0.3 In 0.7 P metamorphic–pseudomorphic high electron mobility transistors on GaAs substrates
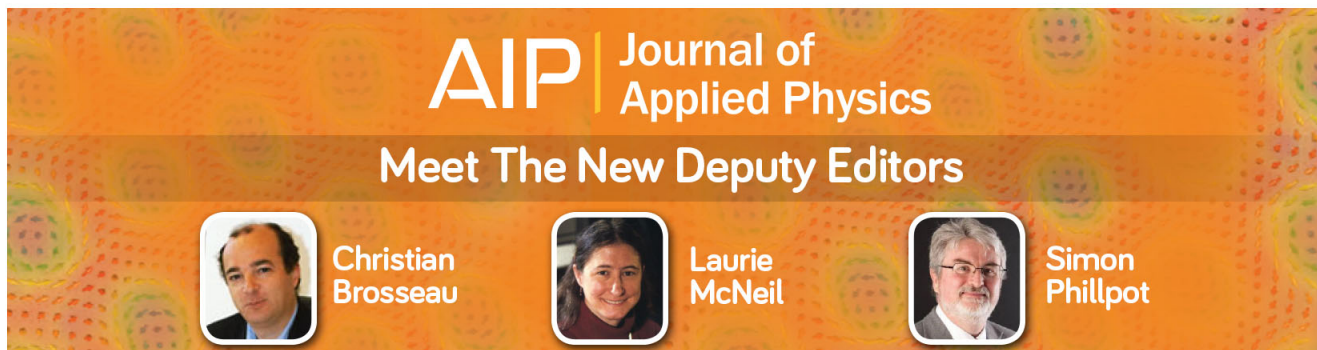J. Vac. Sci. Technol. B 19, 1519 (2001); 10.1116/1.1374629

InGaAsNSb/GaAs quantum wells for 1.55 µm lasers grown by molecular-beam epitaxy
Appl. Phys. Lett. 78, 4068 (2001); 10.1063/1.1379787

Molecular beam epitaxial growth of InAs/AlGaAsSb deep quantum well structures on GaAs substrates
J. Vac. Sci. Technol. B 16, 2644 (1998); 10.1116/1.590249

Strained InGaAs/GaPAsSb heterostructures grown on GaAs (001) for optoelectronic applications in the 1100–1550 nm range

W. Braun,[a)] P. Dowd,[b)] C.-Z. Guo,[c)] S.-L. Chen,[d)] C. M. Ryu,[e)] U. Koelle,[f)]
S. R. Johnson, and Y.-H. Zhang
*Department of Electrical Engineering and Center for Solid State Electronics Research, Arizona State
University, Tempe, Arizona 85287-6206*

J. W. Tomm and T. Elsässer
*Max-Born-Institute for Nonlinear Optics and Short Pulse Spectroscopy, Max-Born-Str. 2 A, D-12489 Berlin,
Germany*

D. J. Smith
*Center for Solid State Science and Department of Physics and Astronomy, Arizona State University, Tempe,
Arizona 85287-1704*

We present a novel semiconductor quantum well (QW) structure consisting of alternating (In,Ga)As and Ga(P,As,Sb) layers grown pseudomorphically on a GaAs substrate by all-solid-source molecular beam epitaxy. The band gap of the QW is determined by the thickness and composition of both types of layers and can be varied from 1.1 to 1.55 μm. Calculations show that the observed strong room-temperature photoluminescence in this wavelength range can be explained by a type-II transition in the QW. Structural investigations by reflection high-energy electron diffraction, transmission electron microscopy, and secondary ion mass spectroscopy confirm a triple layer structure with laterally modulated composition. Photoluminescence measurements reveal a linewidth of 50 meV at 1.3 μm and a luminescence decay time of 240 ps. Our investigations demonstrate the feasibility of this materials system for vertical cavity surface-emitting lasers and other optoelectronic devices on GaAs. © 2000 American Institute of Physics. [S0021-8979(00)03917-7]

I. INTRODUCTION

Vertical-cavity surface-emitting lasers (VCSELs) operating at 1.3 and 1.55 μm are potentially attractive devices for a wide range of applications, such as optical communication, data links, and optical interconnection. In addition to their wavelength matching the dissipation and dispersion minima of optical fibers, such devices would offer a lower operating voltage, allowing their direct integration with low-voltage Si-based integrated circuits.

For the fabrication of such long-wavelength VCSELs, materials need to be found that combine a strong radiative transition at the desired wavelength for the active region with a large difference in refractive index for the Bragg mirrors. Several approaches to this problem are currently being investigated. Whereas the InP/In(Ga,As,P) materials system is the system of choice for edge emitters in this wavelength range,

VCSELs grown monolithically with these materials exhibit poor performance due to the high thermal sensitivity and refractive index properties of the phosphides.[1] One solution is to bond (In,Ga)(As,P) quantum well (QW) active regions to GaAs[2] using wafer fusion techniques. This method has been successfully applied to VCSEL structures,[3,4] resulting in an improved device performance. The main problem with this technique is the wafer fusion process, which is technologically rather difficult and results in high cost per unit.

A single epitaxial growth process on a GaAs substrate is therefore highly desirable. One approach uses quantum dot (QD) structures produced by Stranski–Krastanov growth of (In,Ga)As on GaAs. (In,Ga)As QD structures have shown photoluminescence (PL) at up to 1.35 μm.[5,6] An edge-emitting QD laser has been demonstrated using this active region material.[7] The emission wavelength was 1.31 μm and in order to achieve lasing, a long (2.1 mm) cavity and high reflectivity facet coatings were required. Continuous wave (cw) room temperature operation of an (In,Ga)As QD-based VCSEL has also been achieved,[8] but the lasing wavelength was only 1.15 μm.

Room temperature PL at 1.3 μm has been observed using strained Ga(As,Sb) quantum wells (QWs) and lasing has been reported in an edge-emitting device at 1.27 μm.[9] Using (Ga,In)(N,As) as the active layer material, cw operation of an edge emitting laser at 1.3 μm was achieved in a device where the nitrogen content of the QW was increased to 1%.[10] So far, the approach able to achieve the longest emission

a)Now at Paul–Drude Institute for Solid State Electronics, Hausvogteiplatz 5-7, D-10117 Berlin, Germany; electronic mail: braun@pdi-berlin.de
b)Now at Nanyang Technological University, Department of Electrical and Electronic Engineering, Nanyang Avenue, Singapore 639798.
c)Permanent address: Department of Physics, Peking University, Beijing 100871, China.
d)Permanent address: Department of Applied Mathematics, Tsing Hua University, Beijing, 100084, China.
e)Now at Motorola, 1303 E. Algonquin Rd. IL01/ANX2, Schaumburg, IL 60196.
f)Now at Agilent Technologies, 350 W. Trimble Rd./M.S. 90UB, San Jose, CA 95131.

wavelength in a GaAs-based VCSEL structure used a single (Ga,In)(N,As) QW. Room-temperature (RT) pulsed operation was achieved with an emission wavelength of 1.18 μm and a threshold current density of 3.1 kA/cm^2.[10]

PL up to 1.332 μm has been observed in Ga(As,Sb)/(In,Ga)As bilayer QW samples, with a type-II band-edge alignment.[11,12] Among other advantages,[13] such a type-II band alignment allows more freedom in obtaining a certain operation wavelength of an optoelectronic device, since the composition and strain of *two* materials can be tailored, thereby increasing the degrees of freedom in the device design. Both edge- and surface-emitting lasers have been demonstrated using type-II transitions around 2.2 μm[14,15] and 4 μm.[16]

In this work, we demonstrate a similar approach for the communication wavelength range using (In,Ga)As/Ga(P,As,Sb) QWs grown on GaAs. The samples show strong room-temperature PL in the range of 1100–1550 μm, making these structures ideal candidates for GaAs-based optoelectronic devices for this entire wavelength range.

In the following, we first discuss theoretical considerations that demonstrate the feasibility and high efficiency of such type-II structures. We then continue to describe the molecular beam epitaxy (MBE) growth process using an all solid-source growth chamber, together with the *in situ* and postgrowth structural characterization of the layer structures. The third section covers photoluminescence and electroluminescence measurements, including time-resolved data.

II. ENERGY LEVELS AND GAIN SPECTRA

In order to assess the feasibility of the proposed type-II QW structure and to compare it with matured 1.3 μm (In,Ga)AsP/InP lasers, a well established empirical two-band theoretical model taking into account nonparabolicities in both the conduction and valence bands has been used[17] to calculate the quantum confined energy levels and their corresponding normalized wave functions. Without losing generality, the calculations presented here focus on typical structures consisting of In$_{0.4}$Ga$_{0.6}$As and GaP$_{0.12}$As$_{0.40}$Sb$_{0.48}$ layers (labeled layers A and B, respectively). The critical thickness for the coupled double quantum well (CDQW) structure made of this material system is calculated to be 7 nm based on a single-kink mechanism[18] by the energy balance method. Figure 1 shows the calculated band-edge diagram of a typical CDQW structure with a thickness of 2 and 3 nm for the A and B layers, respectively. Since the band offset between these materials is not well known, the band-edge alignment of the CDQW has been calculated using the model solid theory[19] taking into account strain effects. The band-edge discontinuities and the energy levels of the electron confined states in the conduction band and those of the heavy-hole confined states in the valence band with no injection are plotted to scale. The material parameters used for the theoretical calculations, together with the calculated band offsets are listed in Table I. These calculations indicate that the band-edge alignment of the CDQW structure is type II. The electron barrier is 196 meV at the In$_{0.4}$Ga$_{0.6}$As/GaP$_{0.12}$As$_{0.4}$Sb$_{0.48}$ heterointerface.
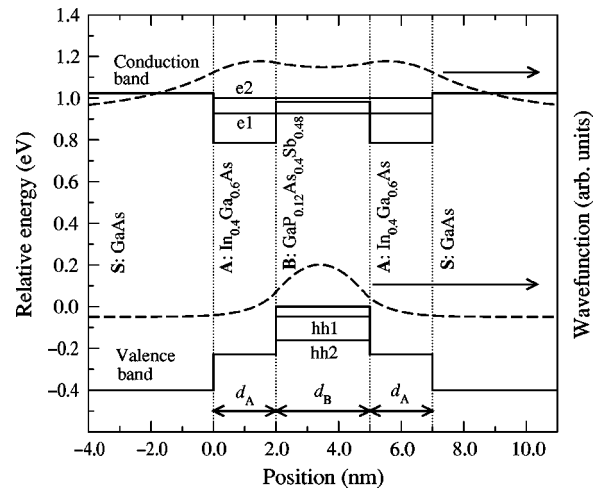

FIG. 1. The band-edge diagram and confined states of electrons and heavy-holes for an In$_{0.4}$Ga$_{0.6}$As/GaP$_{0.12}$As$_{0.4}$Sb$_{0.48}$/In$_{0.4}$Ga$_{0.6}$As CDQW structure with layer thicknesses d$_A$=2 nm and d$_B$=3 nm, embedded in GaAs. The lowest energy-state electron and heavy-hole wave functions are also shown.

The calculated wave functions for both the electron and the hole states in the CDQW are also plotted in Fig. 1. The heavy-hole wave function is strongly localized in layer B due to the heavy-hole effective mass. Since layer B is very thin, has a low electron barrier, and possesses small electron effective mass, the electron wave function can penetrate through it, resulting in strong coupling between the two A [(In,Ga)As] wells. Therefore, there is a substantial part of the electron wave function present in the B [Ga(P,As,Sb)] barrier layer. As a result, the electron- and hole-wave functions have a reasonably large overlap.

For VCSELs, the injection level in the active region can be very high. It is therefore important to take into account band gap shrinkage (band gap renormalization) due to electron–electron, electron–hole, and hole-hole interactions. To obtain a good estimate without going through complicated calculations of these many-body effects, a theoretical model[20] is used to estimate the band gap shrinkage. The additional potential variation across the well region due to the spatially separated charges of electrons and holes is expected to be small for the proposed narrow quantum well and has not been included in our calculation.

To calculate the gain spectra of the strained type-II CDQW structure, an equivalent type-I mixed QW model has been developed. In this model, it is assumed that the coupling between the wells splits every energy level in an isolated well into two, with the total density of states being conserved. The density of states for a coupled energy level in the CDQW is equivalent to that for an energy level in a single quantum well which has the same effective mass and well width as the CDQW structure. This allows the optical transition spectra to be calculated for an equivalent type-I QW in which the electron and hole energy levels have been determined by consideration of the type-II band-edge alignment. As it is found quantitatively that the injected carriers are mainly (more than 90%) populated in the lowest electron and heavy-hole confined states, the densities of states for a symmetrical CDQW can be defined as

TABLE I. Material parameters used for the calculations of an $In_{0.4}Ga_{0.6}As/GaP_{0.12}As_{0.4}Sb_{0.48}/In_{0.4}Ga_{0.6}As$ CDQW structure embedded in GaAs.

Layer	Substrate	A	B
Material	GaAs	$In_{0.4}Ga_{0.6}As$	$GaP_{0.12}As_{0.4}Sb_{0.48}$
Electron effective mass, m_c/m_0	0.067	0.049	0.06
Heavy-hole effective mass, m_h/m_0	0.45	0.434	0.439
Light-hole effective mass, m_l/m_0	0.074	0.056	0.065
Spin-orbital splitting energy, Δ_s (eV)	0.34	0.356	0.539
Refractive index, $\bar{n}_r$	3.409	3.459	3.557
Lattice constant, a (nm)	0.5653	0.5815	0.5841
Strain, ε (%)	0	-2.867	-3.304
Poisson ratio, ν	0.312	0.325	0.302
Electron-heavy-hole band gap, $E_{gh\varepsilon}$ (eV)	1.424	1.017	0.983
Electron-light-hole band gap, $E_{gl\varepsilon}$ (eV)	1.424	1.212	1.201
		Band offsets for different heterointerfaces	
Heterointerfaces	S-A	A-B	S-B
Conduction band offset, $V_{c\varepsilon}$ (eV)	0.237	0.196	0.041
Heavy-hole band offset, $V_{h\varepsilon}$ (eV)	0.171	0.229	0.400
Light-hole band offset, $V_{l\varepsilon}$ (eV)	-0.025	0.207	0.182
Energy gap between A and B bandedges, E_{ch0} (eV)		0.787	
Split between heavy- and light-hole band edges, ΔE_{hl} (eV)		0.217	

$$\rho_{cn}^{QW} = \frac{1}{2}\frac{m_{cA}}{\pi\hbar^2 d_A} + \frac{1}{2}\frac{m_{cA}}{\pi\hbar^2 d_A} = \frac{m_{cA}}{\pi\hbar^2 d_A}, \qquad (2.1)$$

$$\rho_{vn}^{QW} = \frac{m_{vB}}{\pi\hbar^2 d_B}, \qquad v = h,l$$

for the conduction band and the valence bands, respectively, where d_A and d_B are the well (layer A) and barrier (layer B) thicknesses, and m_{cA} and m_{vB} are the electron and hole (including heavy- or light-hole) effective masses in the A and B layers, respectively. The gain spectrum with intraband scattering broadening is given by

$$g(\hbar\omega) = C_g(\hbar\omega) \sum_{n,m} \sum_{v=h,l} \int_{E_{qvn}}^{\infty} |\underline{M}|^2 \rho_{rvn}^{QW}[f_{cn}(E_t)$$
$$- f_{vm}(E_t)]\frac{\frac{1}{\pi}\frac{\hbar}{\tau_{in}}}{(E_{cv}-\hbar\omega)^2 + \left(\frac{\hbar}{\tau_{in}}\right)^2}dE_{cv}, \qquad (2.2)$$

$$r_{sp}(\hbar\omega) = C_r(\hbar\omega) \sum_{n,m} \sum_{v=h,l} \int_{E_{qvn}}^{\infty} |\underline{M}|^2 \rho_{rvn}^{QW} f_{cn}(E_t)$$
$$\times [1-f_{vm}(E_t)]\frac{\frac{1}{\pi}\frac{\hbar}{\tau_{in}}}{(E_{cv}-\hbar\omega)^2 + \left(\frac{\hbar}{\tau_{in}}\right)^2}dE_{cv} \qquad (2.3)$$

in which the prefactors are given by

$$C_g = \frac{\pi q_e^2 \hbar}{c_0 \varepsilon_0 m_0^2} \frac{1}{\bar{n}_r \cdot \hbar\omega},$$

$$C_r = \frac{q_e^2}{\pi c_0^3 \varepsilon_0 m_0^2 \hbar^2} \bar{n}_r \cdot \hbar\omega, \qquad (2.4)$$

$$\bar{n}_r = \frac{2\bar{n}_{rA} + \bar{n}_{rB}}{3},$$

where q_e, c_0, ε_0, m_0, and $\bar{n}_r$ are the electron charge, light velocity, permittivity in vacuum, free electron mass, and refractive index, respectively. f_{cn} and f_{vm} are the Fermi–Dirac distribution functions in the conduction and valence bands, respectively. The optical momentum matrix element will be given approximately by

$$|\underline{M}|^2 = |M_b|^2 F_M |I_{vmB}^{cnA}|^2 \delta_{\underline{k}_{ctA},\underline{k}_{vtB}}, \qquad (2.5)$$

$$I_{vmB}^{cnA} = C_{cvn}\delta_{nm},$$

$$|M_b|^2 = \xi m_0 E_g^{AB}, \qquad (2.6)$$

$$\xi = C_m \frac{E_g^{AB} + \Delta_{sB}}{E_g^{AB} + \frac{2}{3}\Delta_{sB}} \frac{1 - \frac{m_{cA}}{m_0}}{6\frac{m_{cA}}{m_0}},$$

$$F_M = \frac{3}{4}\left(1 + \frac{E_{hmB}}{E_{hmB} + \frac{m_{rh}}{m_{hB}}E_t}\right),$$

where $C_m \approx 1.27$,[21] and I_{vmB}^{cnA} is the interband interlayer electron and hole wave function overlap integral with value C_{cvn} for $m = n$. Here, E_g^{AB} is the bandgap including the effect of shrinkage. F_M is the polarization-dependent factor for the TE mode. It is important to emphasize that the larger the electron and hole wave function overlap I_{vmB}^{cnA}, the larger the momentum matrix element and the material gain, as shown in Eqs. (2.2) and (2.6). It is therefore desirable to choose the structure with the largest wave function overlap.
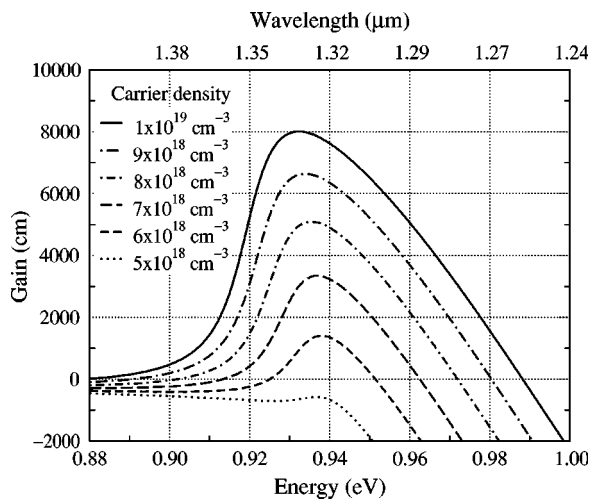
FIG. 2. The calculated TE mode material gain spectra for a 2 nm-3 nm-2 nm structure as a function of carrier concentration.

Calculated gain spectra under different injection levels are shown in Fig. 2 for a structure with $d_A = 2.0$ nm and $d_B = 3.0$ nm. In this case, the transparency carrier concentration is calculated to be approximately 5.3×10^{18} cm^{-3}. The maximum value of the gain peak is $8\,008$ cm^{-1} under a carrier injection of 10^{19} cm^{-3} and occurs at a wavelength of 1.33 μm. This carrier concentration is not unreasonable for the operation of VCSELs.

III. SAMPLE PREPARATION

Based on these calculations, we designed, grew, and characterized samples consisting of typically three successive QW layers embedded in GaAs. The layer sequence was (In,Ga)As–Ga(P,As,Sb)–(In,Ga)As with individual QW thicknesses of approximately 3 nm. The target In composition was around $\approx 30\%$, so that the thickness of the combined structure was below the calculated critical thickness of 10–20 nm, depending on the Sb content. The maximum strain per layer was calculated to be less than 3%. Both the In content in the electron confinement layer and the P:As:Sb ratio in the hole confinement layer were varied systematically to obtain different transition wavelengths.

A. MBE growth

All samples were grown by molecular beam epitaxy (MBE) on 2 in. GaAs substrates. We used the double-chamber system at Arizona State University in which one of the growth chambers (B) was equipped with solid source valved cracker cells for As, Sb, and P. The second growth chamber A, accessible from chamber B through a ultrahigh vacuum (UHV) transfer tunnel, was equipped for high-uniformity growth using Al, Ga, In, and As with Be and Si as dopants.

The growth temperature for the active region layer stack was 505 °C, the remaining GaAs/AlGaAs growth being done at typical growth temperatures around 580 °C. We did not observe any significant difference between overgrowth at 505 or 580 °C as long as the initial capping of the active layer was done at 505 °C. The samples for PL measurements

were deposited on top of a 20-period AlAs–GaAs superlattice followed by a 220 nm GaAs buffer layer, and they were capped by a 10-nm-thick GaAs layer. A special sample with a thinner cap layer was grown for high-resolution secondary ion mass spectroscopy (SIMS) measurements. Additionally, an edge emitting light emitting diode (LED) was fabricated using the UHV transfer capabilities of the MBE machine. Both the top and bottom AlGaAs cladding layers were deposited in chamber A while the QW region was grown in chamber B with a total of two intergrowth UHV transfers.

Chamber B was equipped with all solid sources for Ga, Al, In, As, Sb, and P. Additional dopant cells were not used in this study. For As, Sb, and P, valved cracker sources were used with the cracking zones set at 900 (As), 1000 (Sb), and 900 °C (P). This resulted in a large fraction of dimers in the molecular beams of these group V cells. The Ga growth rate was determined from reflection high-energy electron diffraction (RHEED) intensity oscillations during substrate rotation.[22] (In,Ga)As growth rates were inferred from RHEED oscillations on InAs, which are usually less accurate than in the GaAs case.

The group V source fluxes could not be quantitatively determined in the growth chamber since the flux measurement gauge of chamber B was not operational at the time of the growths. Typical background pressures measured roughly opposite the P cell and at a right angle to the As cell with the Sb cell at an intermediate position were 2.3×10^{-8} mbar during (In,Ga)As deposition and 9×10^{-9} mbar during growth of the Ga(P,As,Sb) layer.

To grow the mixed group V structure, shutters in front of the Sb and P cells were used in addition to changing the valve positions. A timing diagram for the growth of the trilayer stack is shown in Fig. 3. The Ga(P,As,Sb) growth was separated from the (In,Ga)As by 32 and 34 s growth interruptions, in which the surface was soaked with the group V fluxes of the following layer. Sb is known to preferentially incorporate into a nongrowing surface and replace the As.[23] This behavior may be modified by the additional presence of a P flux in the present case, but we have to take into account that the central layer may be thicker than nominally expected.

The valve positions during Ga(P,As,Sb) growth for the samples discussed in this work are given in Table II. The As data refer to the As valve position during growth of the Ga-(P,As,Sb) layer, all (In,Ga)As layers were grown with a setting of 130. By varying the fluxes of In in the outer layers and the group V fluxes of the central layer, we were able to vary the resulting peak PL wavelength from 1.15 to 1.55 μm. The dependence of PL wavelength on the Sb:P valve position ratio is shown in Fig. 4 for the values of Table II. All data marked by solid lines were taken with the same Sb valve setting, which means that the As:Sb ratio and the sum of the As and Sb fluxes were constant, and only the P flux was varied. For the data marked by thinner lines, the Sb setting was lower, resulting in a higher relative As content of the central layer. These two samples had nominally identical Ga(P,As,Sb) layers and only the In content of the outer layers was varied, resulting in the observed wavelength shift. Generally, increasing the Sb:P ratio led to longer wave-
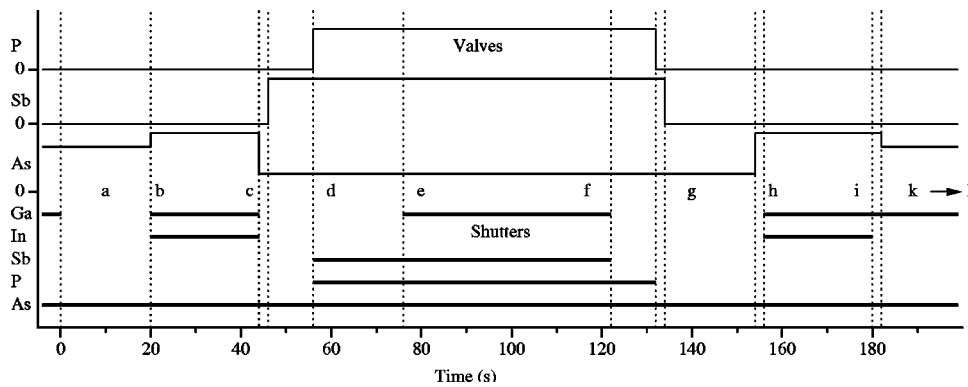
FIG. 3. Timing sequence for the shutters and valves during growth of the active layer. Shutters in front of the valved cells are used in addition to the valves to increase the dynamic range of the molecular fluxes.

lengths. The trend cannot be extrapolated, however, since with (In,Ga)As/GaAsSb/(In,Ga)As samples (without P), the maximum wavelength we obtained was 1.24 μm.

During growth, we recorded RHEED snapshots from the rotating sample, usually close to the $[\bar{1}10]$ azimuth. The results for two samples, B126 and B124, are displayed in Fig. 5. The letters indicate the position of each panel in the growth sequence of Fig. 3. The two different samples differed in their Sb–to–P ratio (see Table II), which was 5 for B126 and 8.3 for B124. For good reproduction in print, the intensity grayscale within each subpanel is normalized to its maximum. This means that the contrast in each panel is an indication of the relative peak intensity: low contrast panels indicate low intensity of the diffraction peak, high contrast panels mean high intensity of the diffraction peak. The high contrast panels therefore correspond to a more ordered surface in the sense that the surface morphology is of regular periodicity. The low contrast panels indicate irregular arrangements of surface atoms with weak correlations.

An additional indication for the varying surface morphology during growth is the position of the main diffraction spot in the different panels. The lower position corresponds to the specularly reflected spot, moving slightly up and down during rotation due to substrate wobble. The upper position is the 002 transmission diffraction spot, which is stationary because it is locked to the direction of the primary beam by the diffraction condition. Transmission spots appear if elevated surface features are present that have a lateral dimension smaller than the extinction length of the electrons. Comparisons between RHEED diffraction patterns and atomic force microscopy (AFM) images[24] demonstrate that this transition can appear for as little as 2 monolayers of deposited mismatched material with a modulation amplitude below 1 nm. The typical chevron shape of (In,Ga)As Stranski–Krastanov growth is present in both the bottom and top (In,Ga)As layers of both structures [Fig. 5, B126(c,d,i), B124(c,d,e,i)]. This indicates the presence of a modulated surface morphology at the corresponding moments in the growth sequence.

Very weak diffraction spots, indicated by low contrast in the figure, occur in panels Fig. 5(h) for B126 and Fig. 5(g) and 5(h) for B124. These are the points in the growth sequence where the group-V flux is switched back to arsenic-stable conditions (Fig. 3). The change in group-V flux seems to cause a major rearrangement of the surface, accompanied by strongly increased disorder. Another unusual phenom-

TABLE II. Room temperature PL wavelengths and selected growth parameters of the samples discussed in this work.

|	P_{Valve}	As_{Valve}	Sb_{Valve}	In_{Temp}	λ (μm)
B101	0	100	0	801	1.14
B114	50	40	250	795	1.29–1.32
B115	50	40	250	795	1.31
B116	50	40	250	795	1.24–1.25
B117	50	40	250	795	1.27
B118	50	40	250	796	1.31–1.33
B119	50	40	250	796	-
B120	70	40	250	796	1.20–1.26
B121	70	40	250	796	1.24–1.25
B122	70	40	250	796	1.15–1.16
B123	40	40	250	796	1.36–1.41
B124	30	40	250	796	1.37–1.41
B125	20	40	250	796	1.41–1.55
B126	40	40	200	796	1.49–1.52
B127	40	40	200	790	1.33–1.40
B132	40	40	250	796	1.44–1.49
B133	0	130	0	796	1.12–1.22
B134	40	40	200	785	1.33
B140	40	40	250	796	1.30–1.32[a]

[a]Electroluminescence.
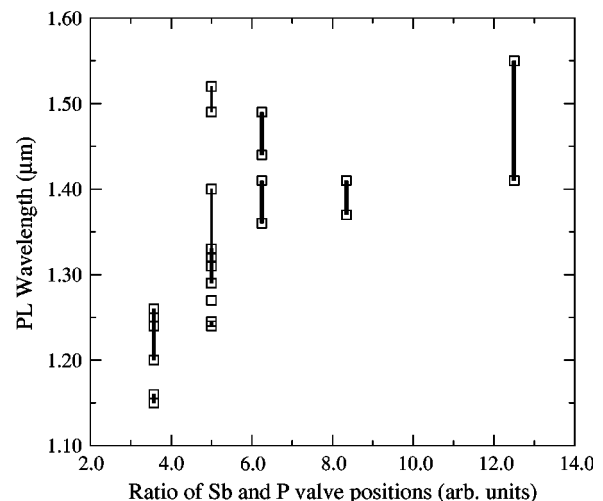
FIG. 4. Dependence of the PL wavelength on the flux ratios during growth of the active layer. The thinner lines indicate samples grown with a different Sb valve setting. The corresponding numerical values can be found in Table II.
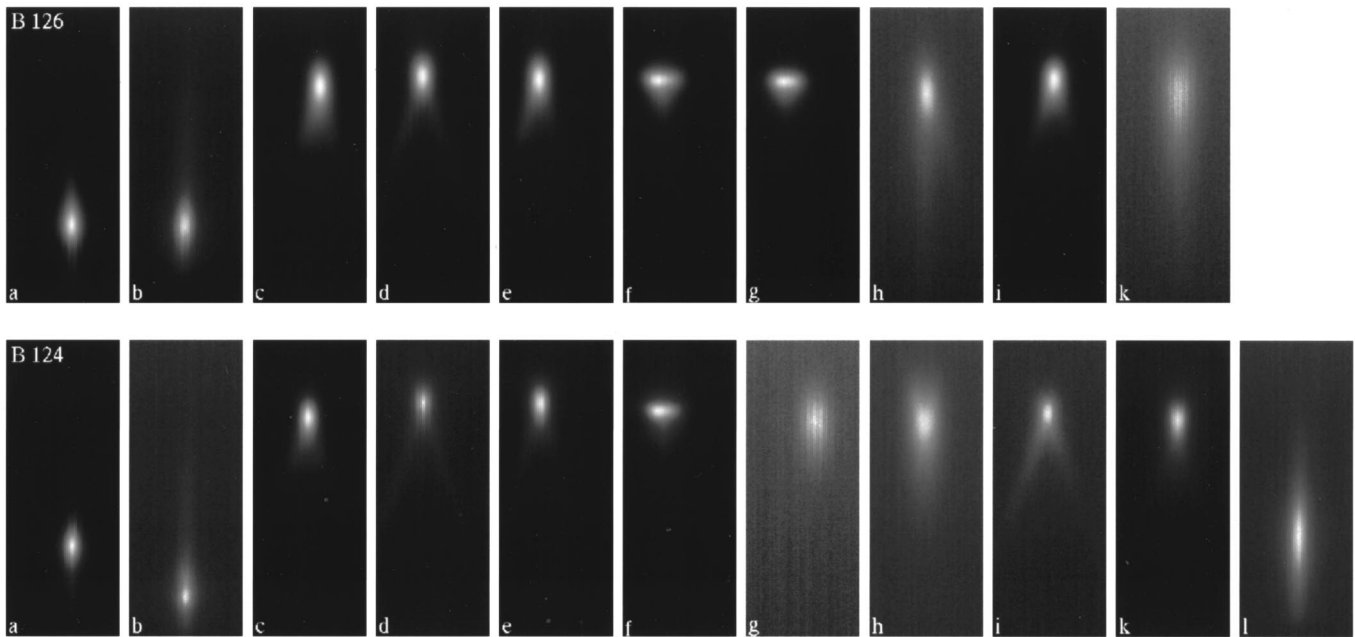
FIG. 5. RHEED diffraction patterns obtained from two samples during growth of the active region. The individual panels show the specular/transmission diffraction spot on the (00) streak at various times indicated by the corresponding letters in Fig. 3.

enon is the special shape of the diffraction spot in Fig. 5(f) and 5(g) for B126 and Fig. 5(f) for B124. In contrast to both the two-dimensional (2D) reflection and the (In,Ga)As layer pattern, the diffraction spot is wider or even split parallel to the surface and more narrow perpendicular to it. At the same time, the contrast is high, indicating good correlation. The diffraction spot, however, is still at the three-dimensional (3D) position, which means that the surface is not flat. The horizontally extended or split peak shape can be explained by lateral domain formation.[25] In such a model, the layer material segregates into volumes with different structure or composition without significant variation of the lattice parameter. The lateral spot size of roughly 1/50 of the Brillouin zone corresponds to a minimum real-space period (domain size) of 50 lattice constants or 20 nm, which agrees well with the average modulation period observed with transmission electron microscopy (TEM) (Fig. 8). A more detailed analysis of the layer structure at this point in the growth sequence is difficult based on the present diffraction data. Spontaneous ordering as the parameter distinguishing the different domains seems rather unlikely, since this usually takes place along the ⟨111⟩ directions. The splitting or broadening, however, is parallel to the sample surface. This would rather point to a compositional modulation parallel to the surface. This may be due to the Ga(P,As,Sb) filling in the valleys of the Stranski–Krastanov template, accumulating on the Stranski–Krastanov mounds, or a more homogeneous deposition where mostly the composition varies. More detailed studies will be needed to clarify this point.

B. SIMS analysis

Several samples were investigated using secondary ion mass spectroscopy (SIMS) to obtain compositional information of the as-grown structures.

Samples B123 and B132 were compared with a dedicated SIMS sample (B134) that was grown with a very thin cap layer to obtain maximum depth resolution. These high-resolution B134 SIMS profiles are shown in Fig. 6. The steepest slopes of all peaks in such a scan represent a lower bound for the resolution of the SIMS. In the present case, these are the surface side shoulders of the phosphorus and antimony peaks. Any slopes that are less steep must therefore be due to structural broadening.

Both the P and the Sb peaks are well localized, indicating that the intended three-layer structure is indeed realized. A slight asymmetry of the phosphorus peak towards the substrate indicates diffusion into the bulk material. In segregates with a diffusion length of 2.2 nm, determined from the
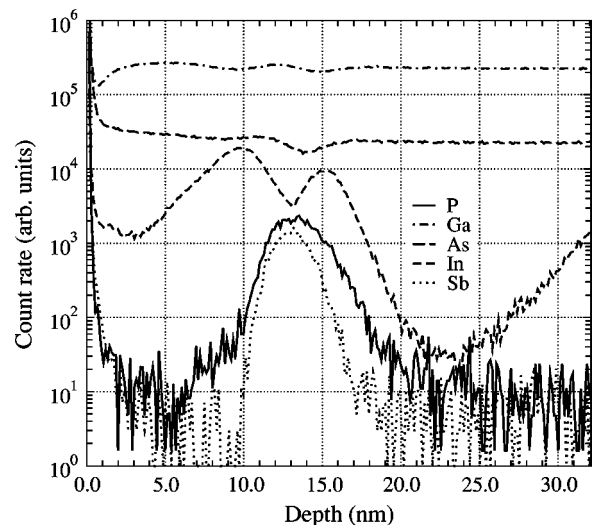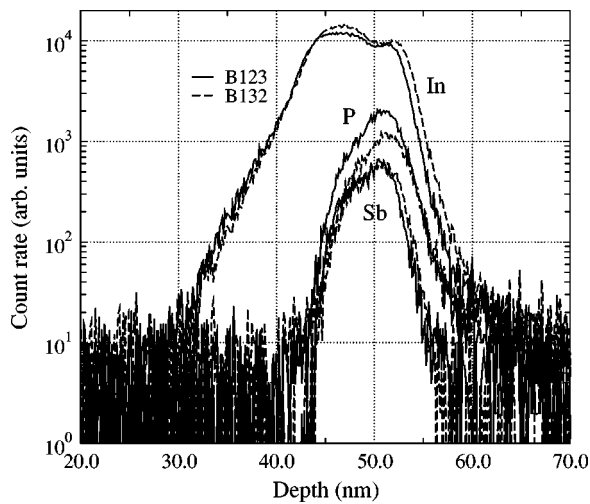

FIG. 6. High-resolution SIMS scan of sample B134.

FIG. 7. Standard resolution SIMS scan of samples B123 and B132.

TABLE III. Ratios of active layer compositions deduced from SIMS measurements.

Sample	In	P	Sb	λ (μm)
123	1	1	1	1.36–1.41
132	1.13	0.63	1	1.44–1.49
134	0.97	0.78	1.25	1.33

the emission wavelength. A change of the P/Sb ratio with slightly lower In content (B134), however, results in a slightly decreased emission wavelength. The basis of three measurement points does not allow us to determine whether strain or composition is the governing factor that defines the emission wavelength.

C. TEM analysis

TEM observations of cross-sectional samples have been carried out to characterize the layer structure and the strain distribution. A cross-sectional view of the active region of sample B114 is shown in Fig. 8. The growth direction was upwards. The QW structure, which is approximately 9 nm wide, can be seen running horizontally through the middle of the image. Strain contrast is clearly visible extending into the GaAs cladding layers on either side of the well. The strain field variations are most probably due to the thickness and compositional variations within the QW itself.

Lattice imaging showed no visible sign of structural defects. Since the image contrast obtained for different group V ions is likely to be similar under high-resolution imaging conditions, the composition within this QW cannot be determined easily. However, the undulating contrast within the QW structure confirms the thickness and composition variations. These variations are consistent with the interpretation of the RHEED oscillation measurements.

IV. OPTICAL CHARACTERIZATION

Temperature-dependent PL measurements have been performed using the 514 nm line of an argon–ion laser at excitation densities up to 1000 W/cm^2. The spectra of a range of samples were obtained using a monochromator and the spectrally resolved signal was detected using a cooled Ge-detector connected to a lock-in amplifier.

shoulder on the surface side of the active layer (4–9 nm depth). A small amount of P seems to segregate along with the In, as can be seen by the low-intensity P peak shoulder between 5 and 10 nm depth. A second period of the active layer was grown underneath the measured structure at ≈ 40 nm depth, resulting in an In shoulder with the same slope that is visible at 25–32 nm depth.

Of the two first-period In peaks, the right one has a steeper slope towards the surface with only about 1 nm segregation length. This coincides with the tendency of P to diffuse in the opposite direction at this interface. At the opposite interface, where (In,Ga)As is grown on Ga(P,As,Sb), the behavior is reversed: whereas P does not segregate, In shows enhanced diffusion back into the Ga(P,As,Sb). The two interfaces within the active layer therefore show a distinct asymmetry in their formation behavior, causing the two (In,Ga)As layers to be different.

The two low-resolution SIMS measurements are shown in Fig. 7. With the lower resolution, the In peaks can no longer be separated and, apart from In segregation, slope differences can no longer be resolved. All peak slopes except for the left side of the indium peak are the same. The clear broadening of the Sb and P peaks towards the sample surface may be due to inhomogeneous segregation of In. This would result in laterally different hardness and therefore different sputtering rates of the cap layer, leading to a rough sputtering front. The softer Ga(P,As,Sb) layer would then be sputtered off the harder underlying (In,Ga)As layer before this layer is attacked, resulting in a smoother sputtering front for the underlying (In,Ga)As.

No calibration standard is available for Ga(P,As,Sb). The present SIMS results can therefore not be directly quantified. The count rates for Ga and As away from the active region stack, however, happen to be the same for all three samples to within the noise levels. This enables us to make quantitative statements about the relative variations of each constituent from sample to sample. The results are shown in Table III, normalized to the composition of sample B123. Increasing the strain from B123 to B132 by increasing the In content and decreasing the P content leads to an increase in
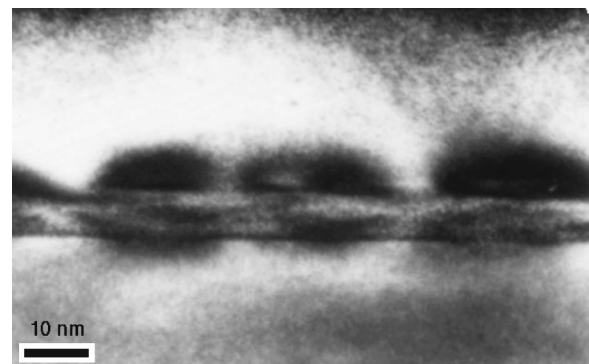

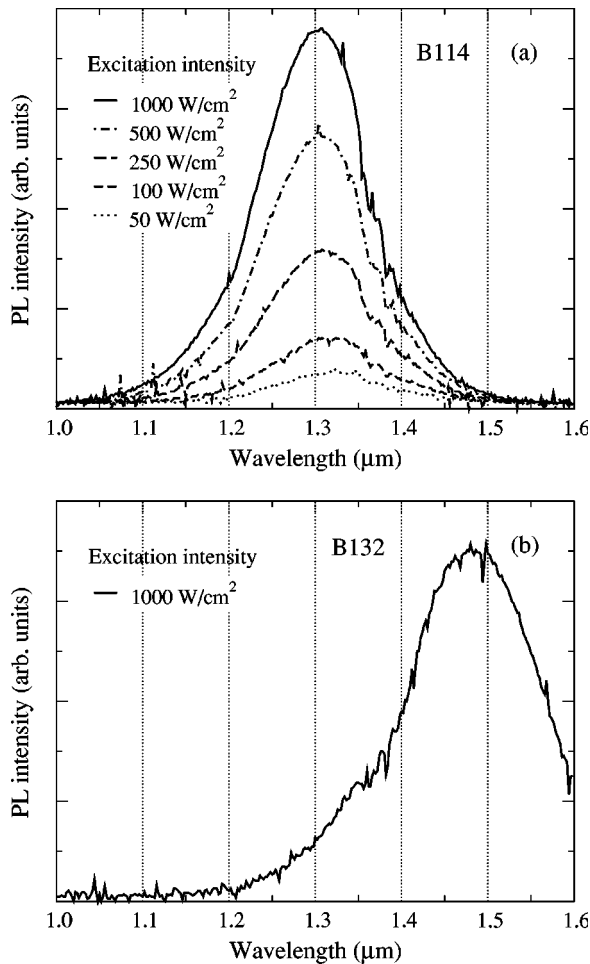FIG. 8. TEM micrograph of the active region (B114).

FIG. 9. Room temperature PL spectra of two different (In,Ga)As/Ga(P,As,Sb)/(In,Ga)As QW structures embedded in GaAs. (a) Sample B114 at different excitation intensities, (b) sample B132 at an excitation intensity of 1000 W/cm^2.

FIG. 10. Linewidth and integrated PL intensity as a function of temperature for sample B114.

A. Photoluminescence

Samples with different compositions for the Ga(P,As,Sb) layer have shown PL emission over a broad wavelength range, extending up to about 1.5 μm at room temperature (RT).

Figure 9 shows the RT PL spectra obtained for two samples. For sample B114 [Fig. 9(a)], the peak of the PL spectrum was observed at 1.3 μm and the linewidth, defined as the full width at half maximum (FWHM), was measured to be 110 meV. As the excitation intensity increased, a blue-shift of the PL spectrum of 13 meV was observed. For sample B132 [Fig. 9(b)], the peak wavelength was close to 1.5 μm, with a FWHM of 130 meV. Additionally it was observed that the peak emission intensity and the integrated emission was weaker than for samples emitting closer to 1.3 μm. For this sample, the Sb:P valve ratio was higher and SIMS also indicates an increased Sb content (see Table III), thus we conclude that more Sb is incorporated in the middle layer of the CDQW. This could increase the valence band offset of the Sb layer, resulting in a narrower effective band gap. A higher Sb content in the layer also causes a larger lattice mismatch between the layer and GaAs. For the increased Sb content, it is therefore possible that dislocations
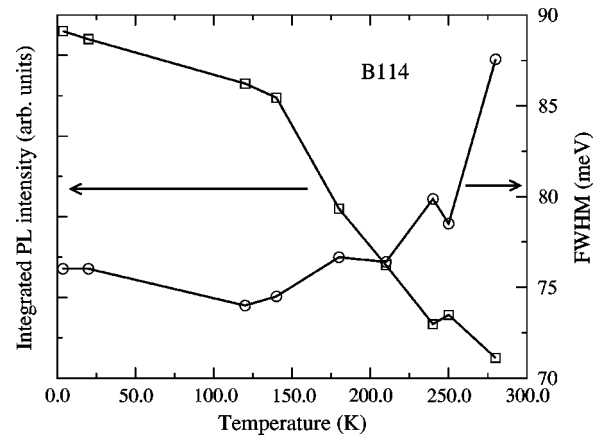
have been introduced into sample B132 that act as nonradiative recombination centers. This could provide an explanation for the reduced emission intensity at this wavelength.

At lower temperatures, the FWHM of the samples decreased and the PL intensity increased. Figure 10 shows the results for sample B114 at an excitation density of about 50 W/cm^2. For temperatures below about 120 K, the linewidth remains roughly constant, with a minimum value of $\approx$ 74 meV. Above this temperature, the linewidth can be seen to broaden. Figure 10 also shows the integrated PL intensity for sample B114.

On decreasing the temperature to 2 K, the intensity increases by a factor of 16. Most of the intensity increase occurs as the temperature is reduced to 120 K. Below this point, the intensity change is considerably smaller.

Figure 11(a) shows the excitation-dependent linewidths for three type-II samples (B114, B116, B129) and one (In,Ga)As sample (B101) at a temperature of 2 K. A minimum linewidth of 50 meV is obtained for sample B129, where the RHEED measurements indicated that the Stranski–Krastanov relaxation of the (In,Ga)As layers was less pronounced. For the (In,Ga)As-only sample, B101, the minimum linewidth is found to be 40 meV.

Figure 11(b) shows the peak emission wavelength of four type-II samples (B114, B116, B123, B129) as a function of the excitation intensity. A large blue-shift of the wavelength of the two (In,Ga)As/Ga(P,As,Sb)/(In,Ga)As samples is clearly visible as the pumping power increases.

As the excitation density is raised from 5 to 250 W/cm^2, a larger blue-shift of the peak wavelength corresponding to 30 meV is observed. This is primarily attributed to the band filling of lower energy states which arise from compositional fluctuations within the GaPAsSb layer. Such blue-shifts have been observed in type-II structures.[12,26] In contrast, the peak wavelength of the (In,Ga)As-only sample is found to be independent of the excitation density for this measurement range.

The broad linewidths of the samples are believed to be dominated by fluctuations in the composition of the Ga(P,As,Sb) layer and the widths of the QW layers,[27] see Secs. III B and III C. Additional linewidth broadening
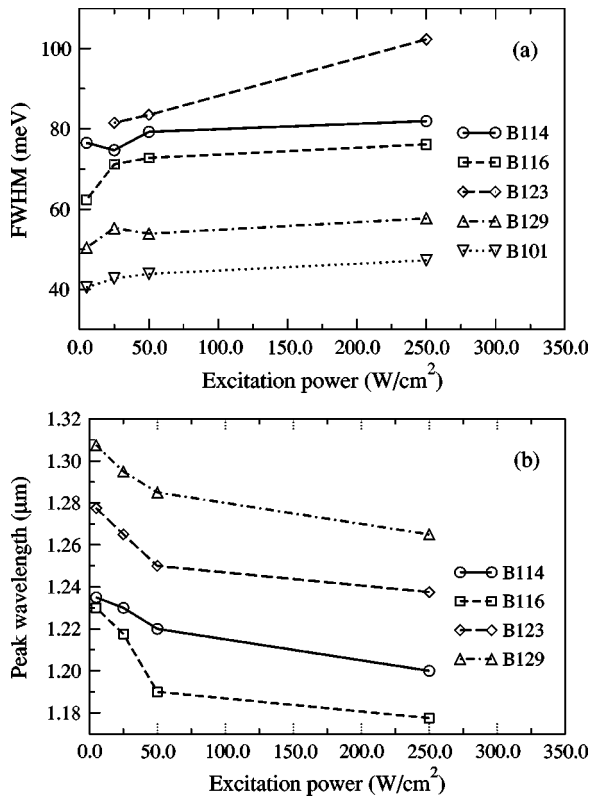
FIG. 11. Linewidths and emission wavelengths as a function of excitation power density for various samples at a temperature of 2 K.
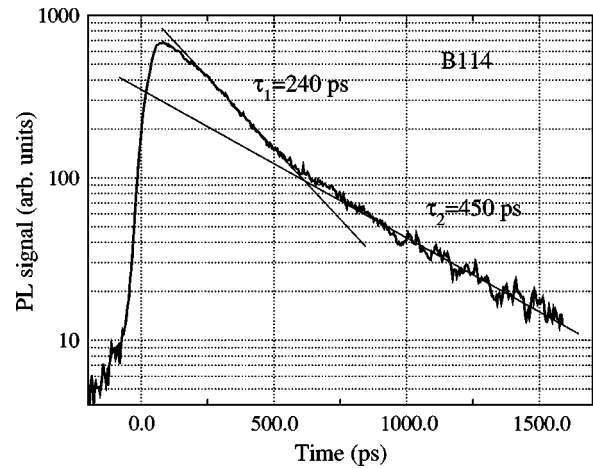

FIG. 12. Transient infrared PL from sample B114. Zero on the time axis was chosen corresponding to the maximum of the excitation pulse.

mechanisms are believed to include (In,Ga)As QW asymmetry resulting from segregation in the growth direction and the strong band-filling effect in type-II structures.[28]

B. Time-resolved photoluminescence

Room-temperature transient PL measurements have been performed with sub-100 fs pulses (λ_{exc}=840 nm, 1.48 eV) at a repetition rate of 82 MHz that were generated by a diode-laser-pumped Cr:LiSAF laser. A streak camera equipped with a cooled charge-couple device (CCD) camera and an infrared-enhanced S1 streak tube (300–1600 nm) were used for detection. The FWHM of the total system response was better than 15 ps. Typical excitation photon fluxes per pulse were on the order of 10^{12}–10^{13} cm^{-2}. Si and other edge filters were used for spectral discrimination.

Samples B114, B123, B126, and B133 were investigated. Out of this series, the longest wavelength sample B126 (cf. Table II) produced the weakest signal. Since the sensitivity of the streak tube is reduced by one order of magnitude from 1300 to 1500 nm, this is most likely due to the tube characteristics.

Figure 12 shows a typical PL transient of the IR emission in the 1050–1500 nm spectral window from sample B114. A biexponential decay with time constants of τ_1 =(240 ± 30) ps and τ_2=(450 ± 50) ps was observed. Within the error limits of the fit, we found a similar behavior for sample B123, whereas both time constants were substantially reduced for the reference sample B133 that basically represents an In$_{0.4}$Ga$_{0.6}$As double QW. Here, τ_1 amounted to about 150 ps, whereas τ_2 was roughly 300 ps. Excitation-

dependent measurements indicated an almost linear dependence for the "slow" (τ_2) and a sublinear (saturation-like) dependence for the fast (τ_1) process.

Since we were not able to separate both carrier decay processes with respect to the spectral position of their emission, a definite assignment is difficult. It is worth to note, however, that all observed τ values are smaller than the 2.5 ns calculated in Sec. II for the spontaneous emission lifetime. Probably, nonradiative processes decrease the PL decay time.

We should mention that we did not observe any infrared emission from the reverse side of the substrate or from uncoated front side regions near the wafer edge. Nonetheless, very strong GaAs PL at about 870 nm ($\tau\approx$ 500 ps) is present in all time-resolved measurements. Despite the fact that PL contributions from the GaAs substrate or cap were eliminated, indirect interference by photon recycling processes cannot be excluded. Thus the slow (τ_2) infrared emission might be excited by reabsorbed GaAs PL.

C. Electroluminescence

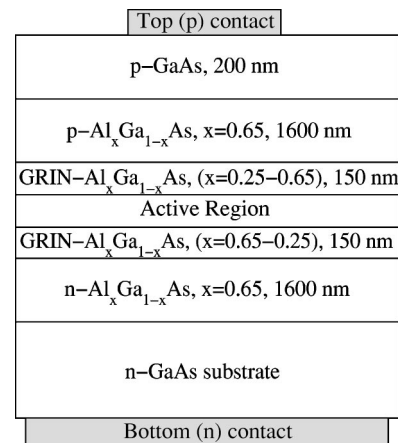In the case of the edge-emitting LED, its schematic structure is shown in Fig. 13. Here, the (In,Ga)As/

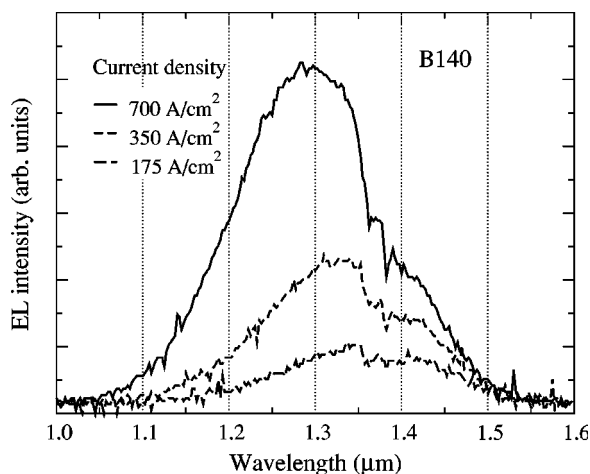
FIG. 13. Schematic structure of the edge-emitting LED.

FIG. 14. Room temperature electroluminescence spectra as a function of current density.

FIG. 16. Temperature-dependent integrated electroluminescence as a function of the current density at various temperatures.

Ga(P,As,Sb)/(In,Ga)As QW region was sandwiched between two doped and graded AlGaAs cladding layers. Devices with a stripe width of 80 μm and a cavity length of approximately 750 μm have been investigated and characterized.

Figure 14 shows room-temperature optical spectra of one of the electrically pumped devices operating at a range of current densities between $\approx$175 to $\approx$700 A/cm^2, corresponding to injection currents of 100–400 mA. The pulse duration was 10 μs, and the duty cycle was 10%. For a maximum injection current of 400 mA (700 A/cm^2), strong EL at close to 1.3 μm was measured. As the injection current was decreased to 200 (350 A/cm^2) and 100 mA (175 A/cm^2), the room-temperature optical spectra shifted to longer wavelengths (approximately 1.325 and 1.35 μm, respectively). The spectral blue-shift at the higher bias currents is primarily attributed to the band filling of lower energy states which arise from thickness and compositional fluctuations within the (In,Ga)As and Ga(P,As,Sb) layers. Gain saturation of the small volume active region may also occur.

Low-temperature measurements have also been carried out and these have revealed a change of the peak wavelength
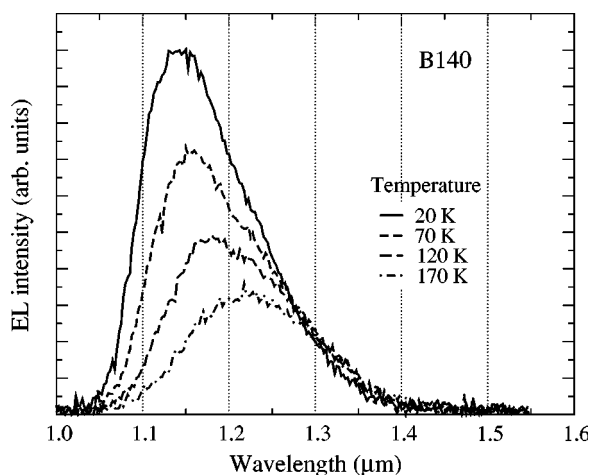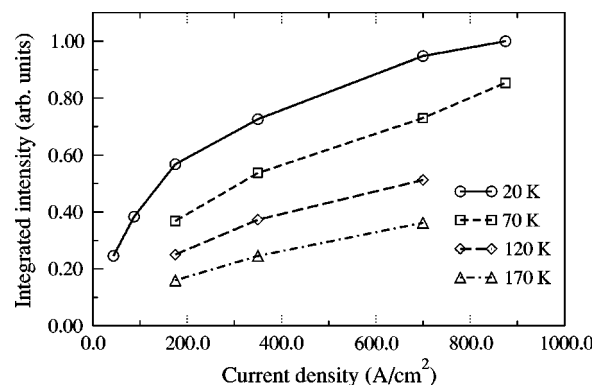
of roughly 3.5 Å /K. Furthermore, as can be seen in Fig. 15, a long-wavelength spectral tail becomes clearly visible. This provides further evidence of a broad range of lower-energy ''tail'' states, caused by the compositional fluctuations in the GaPAsSb layer. A narrowing of the spectral width from about 150 meV at room temperature to 120 meV at 20 K has also been observed.

The integrated EL has been measured and is shown in Fig. 16. For each temperature, the integrated intensity increases as the current density increases. However, it tends to saturate at the higher current densities. On increasing the pulse length or the duty cycle, the integrated output was found to decrease. The saturation is attributed to the fact that there are likely to be a large number of defects in the non-optimized active region of the device. These cause nonradiative recombination to dominate the device performance.

V. CONCLUSION

In conclusion, we have theoretically and experimentally demonstrated a novel layered semiconductor system that allows strong room-temperature emission at 1.1 to 1.55 μm wavelength with devices based on GaAs substrates. The ease of fabrication on GaAs together with the possibility to vary the wavelength across the entire communications wavelength range by only changing the composition of the active layers make this system a promising candidate for the fabrication of optoelectronic devices, and in particular GaAs-based VCSELs. The main problem that needs to be addressed in further research is the relatively broad linewidth of the emission line, which is most probably due to the lateral composition variations in the active region. One challenge will therefore be to grow this structure without approaching the Stranski–Krastanov transition to obtain a two-dimensional geometry.

FIG. 15. Temperature-dependent electroluminescence spectra at 400 mA as a function of temperature.

[1] J. Piprek and S. J. B. Yoo, Electron. Lett. **30**, 866 (1994).
[2] T. Chung, N. Hosoda, T. Suga, and H. Takagi, Appl. Phys. Lett. **72**, 1565 (1998).
[3] J. J. Dudley, D. I. Babic, L. Yang, R. Mirin, B. I. Miller, R. J. Ram, T. Reynolds, E. L. Hu, and J. E. Bowers, Lasers and Electro-Optics Society Annual Meeting, 1993. LEOS '93 Conference Proceedings, IEEE, 1993, pp. 560–561.
[4] J. Behrend *et al.*, J. Cryst. Growth **188**, 295 (1998).
[5] R. P. Mirin *et al.*, Appl. Phys. Lett. **67**, 3795 (1995).
[6] K. Nishi, H. Saito, S. Sugou, and J.-S. Lee, Appl. Phys. Lett. **74**, 1111 (1999).
[7] D. L. Huffaker *et al.*, Appl. Phys. Lett. **73**, 2564 (1998).

[8] D. L. Huffaker, H. Deng, and D. G. Deppe, IEEE Photonics Technol. Lett. **10**, 185 (1998).

[9] M. Yamada, T. Anan, K. Tokutome, K. Nishi, A. Gomyo, S. Sugou, Lasers and Electro-Optics Society Annual Meeting, 1998, LEOS'98, IEEE, Vol. 1, pp. 149–150.

[10] K. Nakahara *et al.*, IEEE Photonics Technol. Lett. **10**, 487 (1998).

[11] M. Peter *et al.*, Appl. Phys. Lett. **67**, 2639 (1995).

[12] M. Peter *et al.*, J. Electron. Mater. **24**, 1551 (1995).

[13] J. Meyer, C. Hoffman, F. Bartoli, and L. Ram-Mohan, Appl. Phys. Lett. **67**, 757 (1996).

[14] A. N. Baranov *et al.*, Electron. Lett. **32**, 2279 (1996).

[15] A. N. Baranov *et al.*, Electron. Lett. **34**, 281 (1998).

[16] J. Malin *et al.*, Appl. Phys. Lett. **68**, 2976 (1996).

[17] D. Nelson, R. C. Miller, and D. Kleinman, Phys. Rev. B **35**, 7770 (1987).

[18] G. Salviati *et al.*, The Proceedings of the 17th Congress on Electron Microscopy, Italian Society, Lecce 2730, 1989 (unpublished).

[19] C. van de Walle, Phys. Rev. B **39**, 1871 (1989).

[20] D. Kleinman and R. Miller, Phys. Rev. B **32**, 2266 (1985).

[21] S. Corzine, R. Yan, and L. Coldren, Appl. Phys. Lett. **57**, 2835 (1990).

[22] W. Braun, H. Möller, and Y.-H. Zhang, Appl. Phys. Lett. **74**, 138 (1999).

[23] F. Hatami *et al.*, Appl. Phys. Lett. **67**, 656 (1995).

[24] B. J. Ohlsson and M. S. Miller, J. Cryst. Growth **188**, 387 (1998).

[25] H. Raether, in *Encyclopedia of Physics*, edited by S. Flügge (Springer, Berlin, 1957), pp. 512–515 (in German).

[26] E. R. Glaser, B. R. Bennett, B. V. Shanabrook, and R. Magno, Appl. Phys. Lett. **68**, 3614 (1996).

[27] A. Chin and W. J. Chen, Appl. Phys. Lett. **69**, 443 (1996).

[28] Y.-H. Zhang, R. Miles, and D. H. Chow, IEEE J. Sel. Top. Quantum Electron. **1**, 749 (1995).